GEOPHYSICS

A rockslide-generated tsunami in a Greenland fjord rang Earth for 9 days

Kristian Svennevig[1]*, Stephen P. Hicks[2], Thomas Forbriger[3], Thomas Lecocq[4], Rudolf Widmer-Schnidrig[5], Anne Mangeney[6], Clément Hibert[7], Niels J. Korsgaard[1], Antoine Lucas[6], Claudio Satriano[6], Robert E. Anthony[8], Aurélien Mordret[9,1], Sven Schippkus[10], Søren Rysgaard[11], Wieter Boone[12], Steven J. Gibbons[13], Kristen L. Cook[9], Sylfest Glimsdal[13], Finn Løvholt[13], Koen Van Noten[4], Jelle D. Assink[14], Alexis Marboeuf[6], Anthony Lomax[15], Kris Vanneste[4], Taka'aki Taira[16], Matteo Spagnolo[17], Raphael De Plaen[4], Paula Koelemeijer[18], Carl Ebeling[19], Andrea Cannata[20,21], William D. Harcourt[17], David G. Cornwell[17], Corentin Caudron[22,23], Piero Poli[24], Pascal Bernard[6], Eric Larose[9], Eleonore Stutzmann[6], Peter H. Voss[1], Bjorn Lund[25], Flavio Cannavo[21], Manuel J. Castro-Díaz[26], Esteban Chaves[27], Trine Dahl-Jensen[1], Nicolas De Pinho Dias[6], Aline Déprez[28], Roeland Develter[12], Douglas Dreger[16], Läslo G. Evers[14,29], Enrique D. Fernández-Nieto[30], Ana M. G. Ferreira[2], Gareth Funning[31], Alice-Agnes Gabriel[19,32], Marc Hendrickx[4], Alan L. Kafka[33], Marie Keiding[1], Jeffrey Kerby[11,34], Shfaqat A. Khan[35], Andreas Kjær Dideriksen[11], Oliver D. Lamb[36], Tine B. Larsen[1], Bradley Lipovsky[37], Ikha Magdalena[38], Jean-Philippe Malet[7,39], Mikkel Myrup[40], Luis Rivera[7], Eugenio Ruiz-Castillo[11], Selina Wetter[6], Bastien Wirtz[7]

Climate change is increasingly predisposing polar regions to large landslides. Tsunamigenic landslides have occurred recently in Greenland (*Kalaallit Nunaat*), but none have been reported from the eastern fjords. In September 2023, we detected the start of a 9-day-long, global 10.88-millihertz (92-second) monochromatic very-long-period (VLP) seismic signal, originating from East Greenland. In this study, we demonstrate how this event started with a glacial thinning–induced rock-ice avalanche of 25×10^6 cubic meters plunging into Dickson Fjord, triggering a 200-meter-high tsunami. Simulations show that the tsunami stabilized into a 7-meter-high long-duration seiche with a frequency (11.45 millihertz) and slow amplitude decay that were nearly identical to the seismic signal. An oscillating, fjord-transverse single force with a maximum amplitude of 5×10^{11} newtons reproduced the seismic amplitudes and their radiation pattern relative to the fjord, demonstrating how a seiche directly caused the 9-day-long seismic signal. Our findings highlight how climate change is causing cascading, hazardous feedbacks between the cryosphere, hydrosphere, and lithosphere.

Steep slopes are prone to destructive landslides that are increasingly likely to occur because of climate change (*1*). In cold regions, this increase may be driven by glacial debuttressing, permafrost degradation, or changes in precipitation (*2*–*5*). A landslide impacting a confined water body, such as a fjord, may produce a destructive tsunami (*6*–*9*), as demonstrated by previously reported events around the globe (e.g., Chile, Alaska, Norway, and Canada) (*8*, *10*–*13*). Similar events have occurred recently in Greenland (*Kalaallit Nunaat*) (*14*–*17*), as exemplified by the 2017 Karrat Fjord event on the west coast (Fig. 1), which caused four fatalities and left two villages permanently abandoned (*17*). However, no such events have previously been observed in East Greenland.

Large landslides are effective sources of long-period (>20 s) seismic radiation owing to their typical long durations (~10 to 100 s), allowing their dynamics to be probed remotely with seismic data (*18*–*20*). The tsunamis induced by such landslides may also produce characteristic seismic signatures, especially in the near field (*21*, *22*). In closed and semienclosed basins, such tsunamis occasionally set up standing waves called seiches (*23*–*25*), in which water sloshes back and forth at a specific resonant frequency. Because their oscillation frequency derives from basin eigenmodes, seiches offer distinctive long-period, monochromatic sources that can be used to remotely investigate energy transfer from the hydrosphere to the solid Earth. Yet so far, only short-duration (<1 hour) loading-induced tilt caused by seiches has been observed on very local (<30-km distance) seismometers (*24*, *26*–*28*). Signals have not been previously recorded at larger distances, and tsunami-induced seiches have not been modeled numerically. Therefore, quantifying how tsunamis and seiches dissipate and radiate elastic waves into the lithosphere remains an open issue further hampered by the lack of high-rate water-level recordings of such events in confined water bodies.

On 16 September 2023, we observed an enigmatic very-long-period (VLP) seismic signal propagating around the globe (Fig. 1A and fig. S1). Unlike broadband earthquake signals, the VLP signal was monochromatic, with a dominant frequency of 10.88 mHz (92-s period), lasting for up to 9 days. Our initial estimates of its source position centered on East Greenland (Fig. 1B) (*29*). At the same time, Greenlandic and Danish authorities received reports of a large tsunami at the (then-unoccupied) Nanok station and research base at Ella Ø (Ella Island) (Fig. 1C). As a rapidly assembled interdisciplinary and international research team, we have integrated local observations, multiscale imagery, regional- to global-scale seismic data, and landslide-tsunami simulations to present a detailed reconstruction of the first documented large tsunamigenic landslide from East Greenland and how it generated a global VLP seismic signal. A high-resolution bathymetry dataset (15-m spacing) in the Dickson Fjord area (fig. S2) (*29*) provided the basis for fine-scale modeling that yields insights into the generation and unusual dynamics of the tsunami.

Field and satellite observations of the landslide

On 16 September 2023 at 12:35 UTC (11:35 local East Greenland time), a 25×10^6 m^3 rockslide (*29*) (supplementary text S1) occurred on

[1]Geological Survey of Denmark and Greenland, Copenhagen, Denmark. [2]Department of Earth Sciences, University College London, London, UK. [3]Geophysical Institute, Karlsruhe Institute of Technology (KIT), Karlsruhe, Germany. [4]Seismology - Gravimetry, Royal Observatory of Belgium, Brussels, Belgium. [5]Institute of Geodesy, University of Stuttgart, Stuttgart, Germany. [6]Université Paris Cité, Institut de Physique du Globe de Paris, CNRS, Paris, France. [7]Institut Terre et Environnement de Strasbourg (ITES), CNRS UMR 7063, Université de Strasbourg, Strasbourg, France. [8]U.S. Geological Survey, Albuquerque, NM, USA. [9]Univ. Grenoble Alpes, Univ. Savoie Mont Blanc, CNRS, IRD, Univ. Gustave Eiffel, ISTerre, Grenoble, France. [10]Institute of Geophysics, Centre for Earth System Research and Sustainability (CEN), Universität Hamburg, Hamburg, Germany. [11]Department of Biology, Arctic Research Centre, Aarhus University, Aarhus, Denmark. [12]Flanders Marine Institute, Oostende, Belgium. [13]Norges Geotekniske Institutt, Oslo, Norway. [14]Royal Netherlands Meteorological Institute (KNMI), De Bilt, Netherlands. [15]ALomax Scientific, Mouans Sartoux, France. [16]Berkeley Seismological Laboratory, University of California Berkeley, Berkeley, CA, USA. [17]School of Geosciences, University of Aberdeen, Aberdeen, UK. [18]Department of Earth Sciences, University of Oxford, Oxford, UK. [19]Scripps Institution of Oceanography, University of California San Diego, La Jolla, CA, USA. [20]Università di Catania, Dipartimento di Scienze Biologiche, Geologiche e Ambientali – Sezione di Scienze della Terra, Catania, Italy. [21]Istituto Nazionale di Geofisica e Vulcanologia, Osservatorio Etneo – Sezione di Catania, Catania, Italy. [22]Université Libre de Bruxelles, Brussels, Belgium. [23]Wel Research Institute, Wavre, Belgium. [24]University of Padova, Padua, Italy. [25]Department of Earth Sciences, Uppsala University, Sweden. [26]University of Málaga, Málaga, Spain. [27]Volcanological and Seismological Observatory of Costa Rica, OVSICORI-UNA, Heredia, Costa Rica. [28]Data-Terra / Theia, CNRS UAR 2013, Strasbourg, France. [29]Delft University of Technology, Delft, Netherlands. [30]University of Seville, Seville, Spain. [31]University of California, Riverside, Riverside, CA, USA. [32]Ludwig-Maximilians-Universität München, Munich, Germany. [33]Weston Observatory, Boston College, Weston, MA, USA. [34]Scott Polar Research Institute, Department of Geography, University of Cambridge, Cambridge, UK. [35]DTU Space, Technical University of Denmark, Kongens Lyngby, Denmark. [36]GNS Science | Te Pū Ao, Wairakei Research Centre, Taupō, New Zealand. [37]University of Washington, Seattle, WA, USA. [38]Institut Teknologi Bandung, Bandung, Indonesia. [39]Data-Terra / ForM@Ter, CNRS UAR 2013, Strasbourg, France. [40]Greenland National Museum and Archives, Nuuk, Greenland.
*Corresponding author. Email: ksv@geus.dk

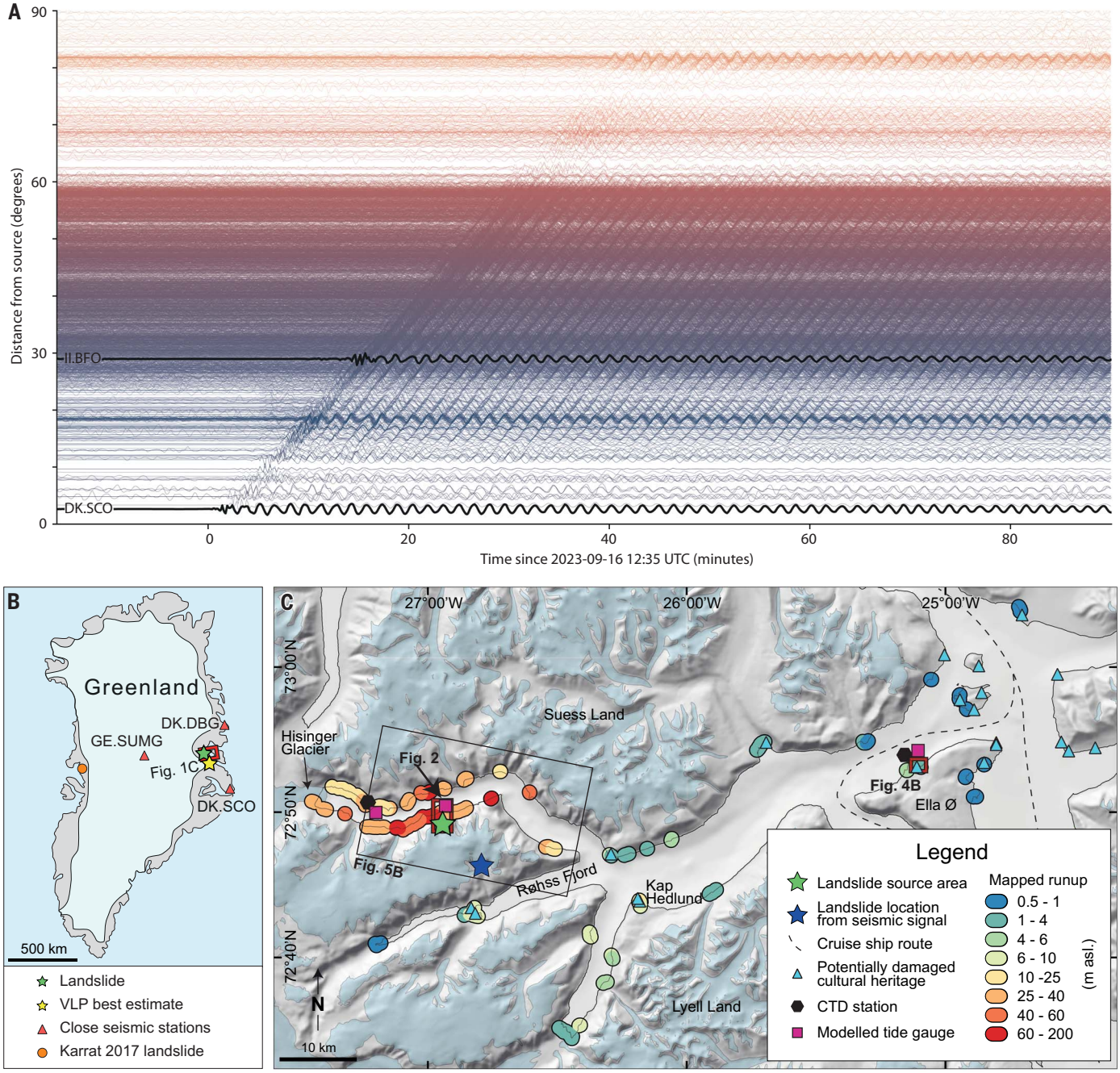

Fig. 1. Seismic signal, position, and local setting. (**A**) Record section showing vertical-component waveforms from ~4,500 seismic stations up to 90° (10,000 km) from Dickson Fjord, with data bandpass filtered at 25 to 115 s and waveforms colored by epicentral distance. Based on the move-out with a phase velocity of 4.1 km/s, these waves can be identified as Rayleigh waves. Stations DK.SCO and II.BFO are highlighted, with detailed views of their waveforms shown in Fig. 5, C and D. A similar but global-scale record section is shown in fig. S1. (**B**) Overview map showing the closest seismic stations, the location of the landslide, and the very-long-period (VLP) seismic source position using waveform back projection (*29*). (**C**) Map of the Dickson Fjord area showing tsunami runup heights and the location of the landslide inferred from both satellite imagery and seismic data. CTD, conductivity, temperature, and depth sensor.

a mountain peak at Hvide Støvhorn 1200 m above Dickson Fjord [Fig. 2, A and B (72.81°N, 26.95°W) and supplementary text S2]. A large body of metamorphic rock (up to 150 m thick, 480 m wide, and 600 m long) dropped westwards along a foliation-parallel failure plane dipping 45° (Fig. 2, D to F, and supplementary text S3). The rockslide impacted and shattered a 200-m-wide outlet glacier in a gully at 600- to 900-m elevation, then turned northward and moved down the 30°- to 40°-steep glaciated gully as a rock-ice avalanche (supplementary text S1), entraining ~2.2 × 10^6 m^3 of the uppermost ~13 m of the glacier (Fig. 2G) (*29*). An 80 m by 220 m peninsula that supported the glacier's calving front disappeared (Figs. 2B and 3A), indicating that the rock-ice avalanche may have triggered a submarine landslide in a sediment cone deposited at the terminus of the gully glacier. On the basis of the fjord morphology from available elevation

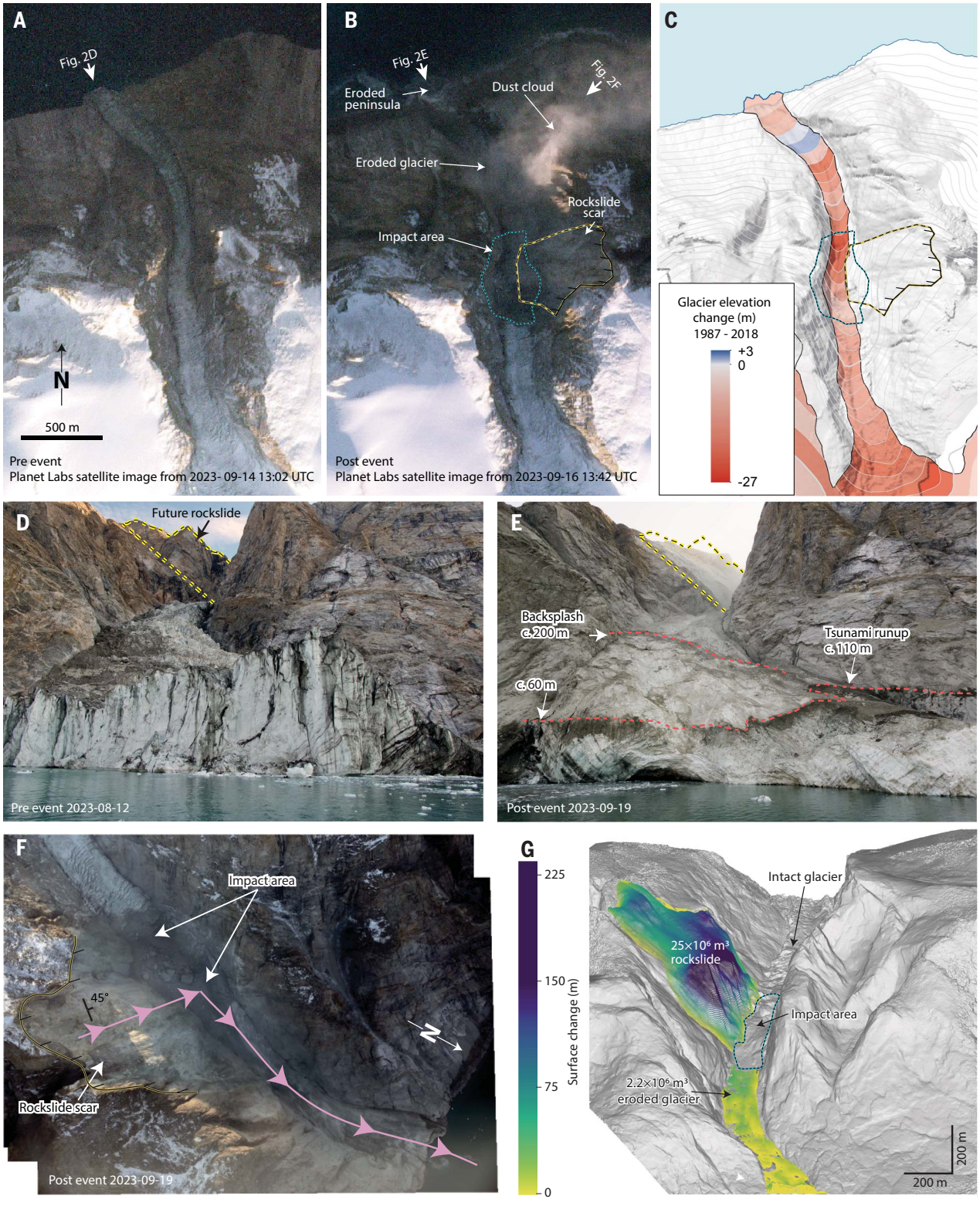

Fig. 2. Landslide observations. (**A**) Pre-event and (**B**) postevent Planet Labs satellite image (locations in Fig. 1C) [Image © 2023 Planet Labs PBC]. (**C**) Mean elevation change during 1985–2018 of the glacier surface per 50-m elevation interval. Scale and field of view are the same for (A) to (C). (**D** and **E**) Pre- and postevent field photos of the coastal slope [looking south, refer to arrows in (A) and (B)]. The stippled yellow line outlines the rockslide source area [location shown in (A) and (B)]. Tsunami runup heights are indicated with stippled red lines in (E) [Source of (E): Sirius Dog Sled Patrol of the Joint Arctic Command]. (**F**) Postevent aerial photomosaic from 19 September 2023 of the onshore landslide-affected area [location shown in (B)] [Source: Joint Arctic Command of the Danish Navy]. (**G**) Orthogonal projection (southward view) of the structure from motion point cloud (*29*), showing the failed bedrock volume and the entrained volume of the glacier below the impact area (stippled blue outline).

models (fig. S2) (*29*), we estimate a minimum total rock-ice avalanche runout distance of 2.2 km.

The lower part of the rockslide failure plane extends beneath the preslide surface of the glacier (Fig. 2, F and G), which had been thinning over the past decades (Fig. 2C) (*29*). We propose that this thinning led to debuttressing of the lower part of the unstable slope, triggering the rockslide. Such dynamic preconditioning is reported for other high-latitude and alpine landslides (*30*, *31*).

In addition to the 16 September 2023 event, we found evidence in satellite imagery of at least four smaller previous landslides and a subsequent one from the same gully (supplementary text S4 and table S1).

Landslide dynamics from seismic inversion

The 16 September 2023 landslide-tsunami event generated substantial seismic ground motions. At nearby stations (e.g., DK.SCO, 300 km away; Fig. 1B), we observed an emergent 200-s-duration high-frequency (HF) (2- to 10-Hz) arrival with an extended coda, accompanied by a 60-s duration signal at lower frequencies (LF) (17 to 100 mHz). The 10.88-mHz VLP signal emerges from these higher-frequency signals (Fig. 3B).

The cigar-shaped HF signal contains two wavetrains. The first signal corresponds to the initial rockslide and the second to the rock-ice avalanche moving down the glacial tongue and entering Dickson Fjord. These waveform characteristics are typical of landslides (*20*), particularly those involving glacial ice entrainment (*18*, *20*, *32*), topographic obstacles, and water bodies (*33*–*35*). The LF waves come from acceleration and deceleration of the bulk mass on the Earth's surface, whereas the HF waves come from interactions between grains in the moving mass with the substrate (*20*, *36*). We used different methods (arrival time inversion, centroid moment tensor waveform inversion, and cross-correlation) to show that the source, which originated at 16 September 2023 12:35:03 UTC, is consistent with the imagery-derived landslide location, with most computed positions within 20-km distance (fig. S3 and table S2). The landslide was sufficiently energetic to produce acoustic signals recorded on International Monitoring System (IMS) infrasound arrays up to 3310 km away (I37NO and I43RU) (*29*).

To estimate the trajectory of the force imparted by the landslide on the Earth's surface, we inverted waveforms from the three-closest seismic stations (Fig. 1B), bandpass filtered between 17 and 100 mHz (*18*–*21*, *29*) (Fig. 3B). Our inversion yields a maximum force of 192×10^9 N, corresponding to a mass of approximately 78×10^9 to 103×10^9 kg, equivalent to a volume of 29×10^6 to 38×10^6 m^3 (assuming a density of 2.70 g cm^{-3}) (*19*, *21*). From the fjord morphology, we estimate a minimum total runout distance of 2.2 km. On the basis of this assumption, the kinematic quantities derived from the inverted force give a 55×10^9 kg mass ($\sim 20 \times 10^6$ m^3), which is consistent with the structure from motion volume reconstruction (*29*). The rock-ice avalanche had a peak acceleration of 3.5 m s^{-2} at 42 s and a peak velocity of 47 m s^{-1} at 52 s after it initiated (Fig. 3D). We find

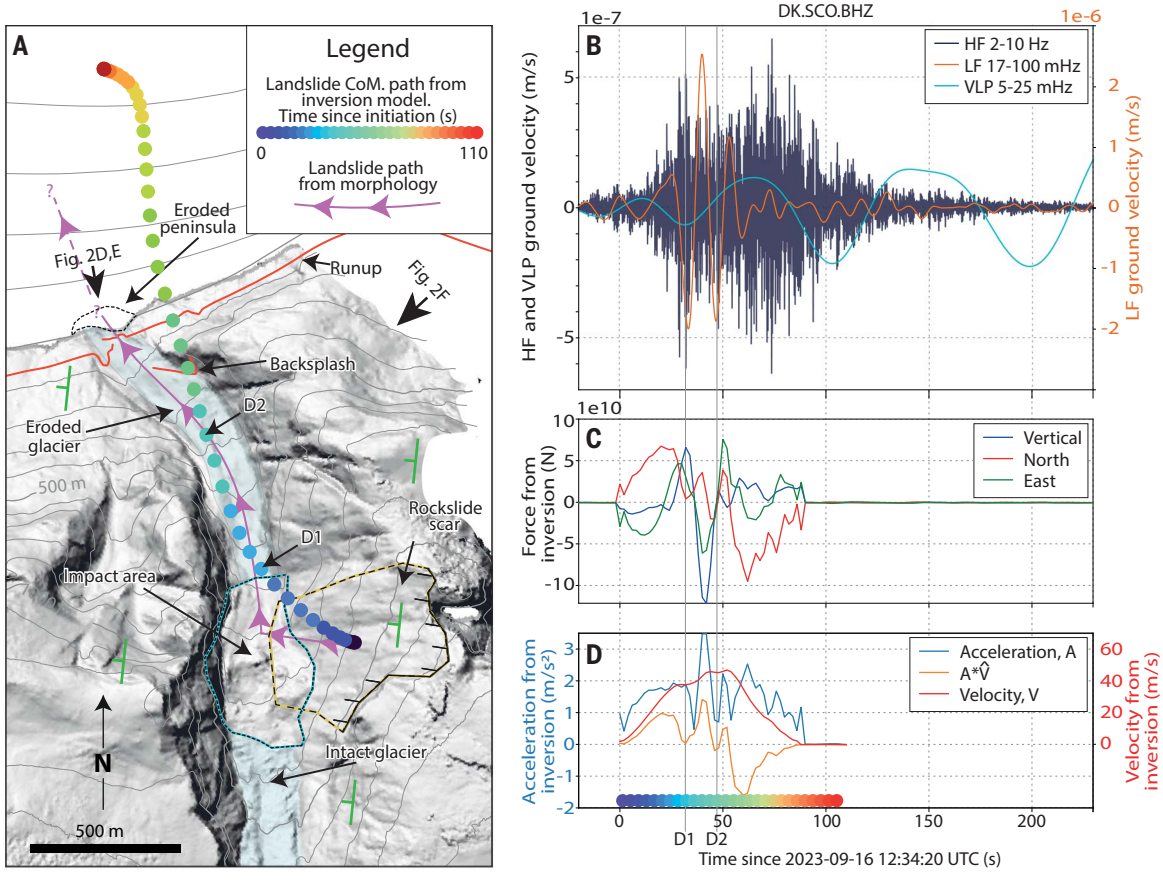

Fig. 3. Landslide seismic signal and modeling. (**A**) Geomorphological map showing the landslide center-of-mass (CoM) runout paths from morphological interpretation and seismic inversion. Green symbols indicate the strike and dip direction of the foliation. (**B**) The seismic signal recorded at DK.SCO.BHZ (313-km distance), shifted by the travel time between the source location and the station (at 3 km/s velocity), with different bandpass filters applied. (**C**) The seismically inverted force of the landslide CoM acting on the Earth. (**D**) Modulus of the seismically inverted acceleration (blue), velocity (red), and scalar product of the acceleration and the normalized velocity ($\hat{v}$; orange) of the CoM of the moving mass; D1 and D2 indicate the two first peaks of deceleration and are shown on the map in (A). The color bar is the same as shown in (A).

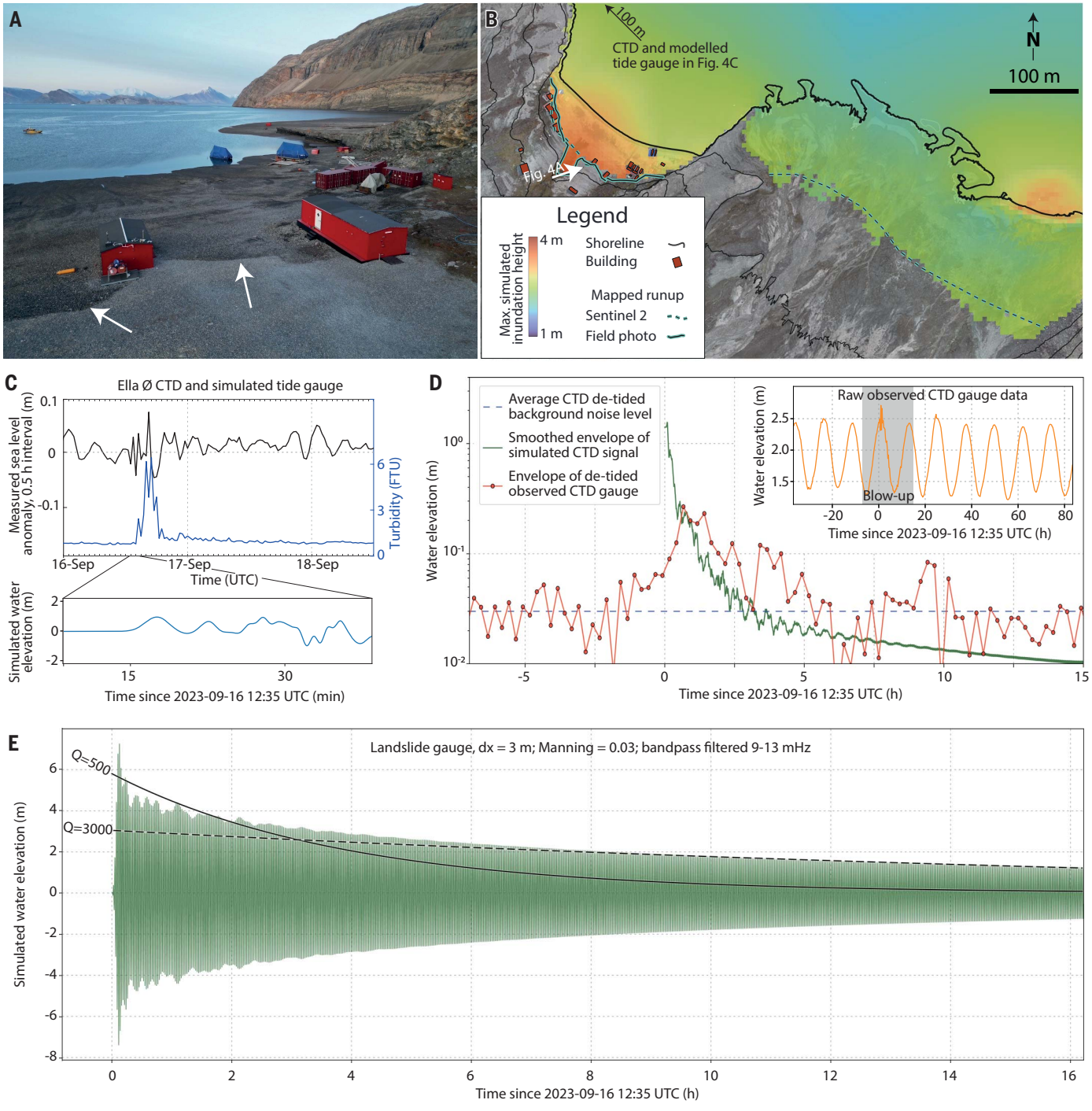

Fig. 4. Tsunami observations and modeling. (**A**) Drone photo looking east-northeast showing the 4-m runup height at Ella Ø (white arrows) [Source: Joint Arctic Command/Sirius of the Danish Navy]. (**B**) Mapped and simulated tsunami runup at Ella Ø. (**C**) Observed and simulated tsunami at Ella Ø using the GloBouss tsunami model (*43*) (Fig. 1C). (Top) Sea level and turbidity from the conductivity, temperature, and depth (CTD) station. FTU, formazin turbidity units. (**D**) Comparison between observed (15-min sampling interval) and simulated (using the HySEA tsunami model) water level at the Dickson Fjord sea-level gauge/CTD station (Figs. 1C and 5B). (**E**) Filtered (9- to 13-mHz bandpass) simulated long-term tsunami water elevation at the landslide-fjord impact location, with indicative exponential decay rates labeled as *Q*-values. The seiche amplitude spectrum is shown in Fig. 5E.

two sudden, mid-path acceleration drops along the direction of movement before the final one ("D1" and "D2" in Fig. 3D), the first coinciding with the maximum of the upward vertical force and both with drops in the north force (Fig. 3C). D1 coincides with an amplitude peak in the HF signal, and D2 marks the onset of the second phase of the HF signal (Fig. 3B), showing the influence of topography (*34*). D1 is likely associated with the mass impacting the west wall; D2 likely corresponds to the moment when the front of the rock-ice avalanche

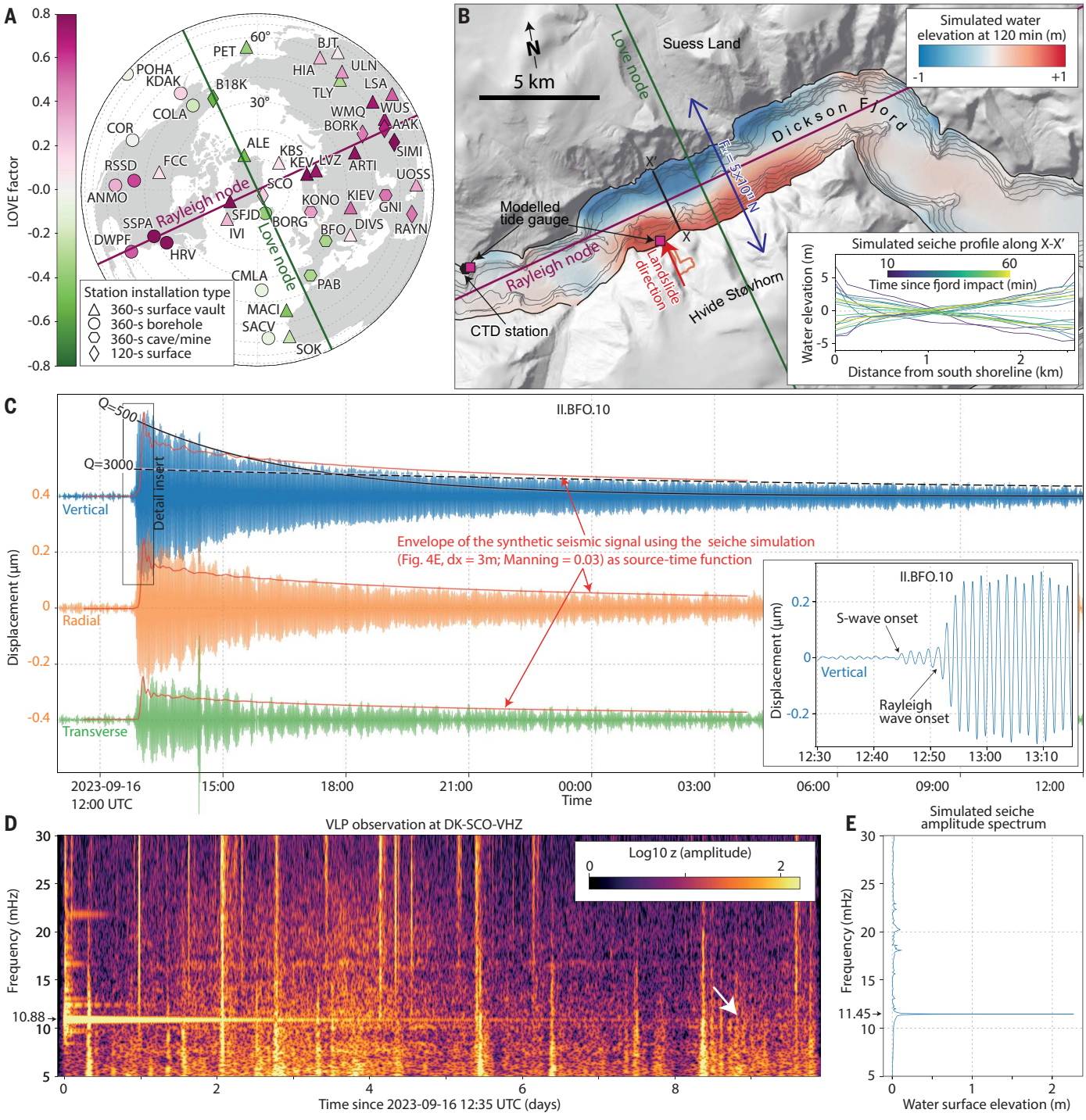

Fig. 5. VLP seismic signal and comparison with simulated seiche. (**A**) Locations of seismic stations with high-fidelity three-component VLP recordings, colored by dominant surface wave type (green, Rayleigh; pink, Love) (*29*). This radiation pattern matches the strike of Dickson Fjord and its perpendicular, as shown in (**B**), where the background red-to-blue colors show a snapshot of the simulated seiche after 2 hours, along with the modeled direction of the oscillating horizontal single force (blue double arrow). (Inset) Simulated seiche profile along X-X′, at different timesteps. (**C**) Waveform recording from station II.BFO in Germany (29° away), showing dominant Rayleigh energy on the vertical and radial components, with weaker Love energy on the transverse. Indicative *Q*-values (black lines) highlight their slow, nonexponential decay. *S* waves arriving at 12:46 UTC (inset) carry the initial VLP signal. Synthetic seismogram envelopes (red lines) using the simulated seiche signal at the location of the landslide (Fig. 4E), scaled to a maximum horizontal force of 5×10^{11} N (*29*), match the maximum VLP amplitudes and their decay. All signals are 10- to 12-mHz bandpass filtered. (**D**) Vertical-component spectrogram from DK.SCO (2.6° away), showing the >9-day-long duration of the VLP signal (white arrow). (**E**) Amplitude spectrum of the simulated seiche time series at the landslide impact in the fjord (Fig. 4E).

reached the water, causing a deceleration to the overall center of mass. Overall, the seismically inverted runout path matches that inferred from imagery (Fig. 3A).

According to our inversion results and morphological observations, the higher-frequency (>25-mHz) seismic waveforms clearly come from the rock-ice avalanche. However, the VLP component of the signal, which emerges out of the higher-frequency waveforms (Fig. 3B), remains unexplained.

Tsunami recordings and modeling

The impact of the 16 September 2023 rock-ice avalanche into the 540-m-deep and 2.7-km-wide Dickson Fjord triggered a tsunami with an initial backsplash with a runup height of ~200 m and subsequent waves up to 110 m high (Fig. 2E) (*29*). The tsunamigenic potential of the rock-ice avalanche was enhanced by its channelization into the gully, the entrainment of ice into the mobilized volume (*18*, *37*), and the glacier lowering the basal friction (*18*, *32*, *35*). At the Nanok station and research base at Ella Ø, 72 km away out-fjord, the tsunami had a local runup height of 4 m, inundating up to 80 m inland, and destroying infrastructure valued at nearly 200,000 USD (Figs. 1C and 4, A and B). Elsewhere in the fjord system, near-coastal cultural heritage sites, such as Thule Culture Inuit archaeological sites and 20th-century trapper huts, were well within the inundation reach and were assumed to be destroyed. The observed destruction of an old trapper hut at Kap Hedlund (Fig. 1C), which had never been affected by tsunamis during its century-old history, demonstrates the historically unprecedented magnitude of the September 2023 event (supplementary text S5). Cruise ships pass east and west of Ella Ø every week in the ice-free season (Fig. 1C), but none were in the fjords during the tsunami.

The tsunami was recorded by nearby pressure sensors and sea-level gauges (*29*, *38*) (Fig. 1C and fig. S18) (*29*). Out-fjord, at Ella Ø, a high turbidity signal was detected resulting from local sediment resuspension by the tsunami, peaking 3 hours after the initial tsunami and lasting 6 to 7 hours (Fig. 4C). The sea level gauge in Dickson Fjord, located 8 km west of the landslide impact point along the shoreline, recorded a maximum peak-to-peak amplitude anomaly of ~0.4 m; however, its 15-min sample interval almost certainly aliases out amplitudes at higher frequencies (Fig. 4D).

We therefore relied on numerical modeling, validated by observed runup heights, to better understand the shorter-period component of the tsunami. We first modeled the tsunami using a linear dispersive Boussinesq model nested with a nonlinear shallow-water inundation model (GloBouss algorithm) (*29*) to simulate the observed inundation, runup height, and the sea-level gauge recording at Ella Ø (adding 0.7-m high-water spring tide at the time of the landslide). The simulated and observed runup heights compare well (Fig. 4, A and B). To verify this result and to better simulate the longer-term evolution of the tsunami within Dickson Fjord, we also used an independent, nonlinear hydrostatic model (*39*) that describes the rock-ice avalanche as a granular flow (*9*) [HySEA (Hyperbolic Systems and Efficient Algorithms) model] (*29*). However, modeling the long-term energy dissipation of tsunamis is a nontrivial task. Unrealistic, artificial damping due to numerical dissipation in complex bathymetric models is inherent in HySEA's finite-volume modeling scheme (*39*–*41*), thus masking realistic physical damping effects, such as out-fjord dissipation and bottom-friction. We indeed observed that numerical dissipation in the finite-volume model masks the effects of bottom friction for grid spacings of >7.5 m, with reduced dissipation in finer grids (fig. S5). This overall result is independently corroborated by GloBouss simulations (supplementary text S6). For our preferred simulation, we therefore used the finest, most computationally feasible grid spacing of 3 m, with a Manning bottom-friction parameter of 0.03, typically used in tsunami modeling (*41*–*43*).

Our preferred simulation setup shows that at ~5 min after the material enters the water, the waves stabilize into a slowly decaying seiche with a maximum amplitude of 7.4 m and a dominant frequency of 11.45 mHz (87 s); (Figs. 4E, 5B, and 5E, and movies S1 and S2). This eigenfrequency is directly related to the width and depth of Dickson Fjord, as shown in the analytical solutions (*42*).

Character of the VLP seismic signal

From the higher-frequency rock-ice avalanche signal (Fig. 3B), a prominent harmonic (monochromatic) signal emerges, with a frequency of 10.88 mHz (92 s), that is observed on seismometers and superconducting gravimeters globally for up to 9 days (Figs. 1A and 5, and fig. S6). The amplitude decay of this VLP signal is extremely slow (Fig. 5C). We quantified this decay by modeling the signal's envelope as $\exp\left(-\frac{t}{T}\frac{\pi}{Q}\right)$, where Q is the quality factor of a harmonic oscillator and T is its dominant period of 92 s (*29*). The initial Q of the signal is ~500, gradually increasing to and stabilizing at ~3,000 (Fig. 5C), indicating a nonexponential amplitude decay. The signal is phase-coherent and undergoes a 540–parts per million semidiurnal frequency modulation for at least its first 50 hours (fig. S7) (*29*).

Our back-projection analysis of global surface waves and regional waveform inversion using a resonating source-time function with an equivalent moment magnitude of 5 found a source location that is stable for 9 days originating from East Greenland near Dickson Fjord (Fig. 1B, table S2, and movie S3) (*29*). However, the long wavelengths at such long periods (~400 km) limit the spatial resolution of these locations. Nevertheless, given that the VLP signal emerges in the coda of the HF signal (Figs. 3B and 5D), we assume it originates near the seismically derived landslide source position from HF waveforms (table S2). However, a landslide lasting several minutes could not have directly generated such a long-duration, slowly decaying, highly monochromatic signal.

Instead, our analysis of three-component seismic waveforms from stations at teleseismic distances shows that the signal's radiation pattern directly relates to the water body in the fjord. We observed predominant Love wave radiation along the longitudinal axis of Dickson Fjord (070°) and Rayleigh wave radiation perpendicular to it (160°; Fig. 5, A and B) (*29*). This pattern mimics the vertical-component signal duration (fig. S8), showing how the VLP signal's observed duration of up to 9 days depends on station azimuth relative to radiation pattern and site-dependent noise level.

Three weeks later, on 11 October 2023, a similar signal that originated from the same location and showed the same fundamental period and radiation pattern, but with half the amplitude, was also observed globally. The signal was also associated with a landslide-tsunami event originating from the same gully with around half the vertical tsunami runup (supplementary text S4). A systematic search of past seismic data (1990–2023) and gravimeter data (1982–1994) from station II.ALE in northern Canada revealed four additional smaller-amplitude, shorter-duration VLP signals with almost identical frequency (fig. S13). At least two of these events (February 2016 and January 2017) were associated with a rock-ice avalanche in the same gully, and, intriguingly, occurred when the fjord was ice-covered.

Although global seismic networks would have been sensitive enough to record them for at least three decades (*44*, *45*), similarly high-amplitude, globally observable, slowly decaying signals with a stable monochromatic period starting at the signal onset are extremely rare. The handful of documented cases with dominant frequencies of >1 mHz have been related to volcanic activity, either through resonance excited by subsurface magmatism (*46*, *47*) or from explosive eruptions exciting the fundamental mode of Earth's atmosphere (~3.7 mHz) (*48*, *49*). In contrast, the Greenland VLP signals have a much slower decay and a different radiation pattern, making them different from previous observations.

A seiche as the source of the global VLP seismic signal

The VLP signal's radiation pattern and slow decay, compared with freely propagating Rayleigh

waves, must be due to its source excitation because no high-Q Earth normal modes exist near 10.88 mHz (*50*). We thus propose that a freely decaying seiche oscillation in Dickson Fjord generated the observed VLP signals, for four reasons.

First, the numerical tsunami simulation stabilizes into a free seiche oscillation with a dominant frequency of 11.45 mHz (87-s period), which is very close to the 10.88-mHz frequency (92-s period) of the seismic signal (Fig. 5, D and E). We attribute the small difference to unmodeled complexities in the fjord's bathymetry (*42*).

Second, the restoring force of the seiche acts in a direction perpendicular to Dickson Fjord and thus provides a horizontal transfer of momentum to the Earth's crust in that direction. This is consistent with the observed radiation pattern of Rayleigh and Love waves (Fig. 5, A and B).

Third, global seismic waveform modeling shows that an oscillating horizontal single force perpendicular to Dickson Fjord with an initial amplitude of 5×10^{11} N (*29*) reproduces the observed ground motion amplitudes and radiation pattern. A horizontal oscillation of the center of mass of the water body in Dickson Fjord of about 14-m amplitude along a section of 10-km length would provide a transfer of momentum equivalent to this force amplitude at a frequency of 10.88 mHz. On the basis of a simplified geometry of the fjord, we expect this horizontal displacement of the center of mass for a vertical seiche amplitude of about 9 m at the surface (*29*), close to the 7.4 m predicted by the seiche simulation (Fig. 4E).

Fourth, the simulated free seiche oscillation shows a decay similar to that of the VLP signal. The seiche has a nonexponential decay, starting at a higher decay rate of Q ~500, and over a few hours gradually transitions to a slower decay of Q ~3000 (Fig. 4E), matching very closely the decay of the VLP signal (Fig. 5C). Such a slowly dissipating seiche is predicted by two different modeling approaches, which are complementary and independent in terms of the physical processes involved and the numerical methods used. From our tsunami simulation with a fine grid spacing (i.e., 3 m, Manning 0.03), we use the near-landslide time series of the seiche (Fig. 4E) to generate a source-time function as input to the global seismic waveform modeling (*29*). The amplitudes, radiation pattern, and signal envelopes of the resulting synthetic seismograms are shown in Fig. 5C together with the recorded waveforms. The good match between synthetics and recordings corroborates the free seiche as the source of the VLP signal.

The freely decaying seiche oscillation in Dickson Fjord

Although a real-time conductivity, temperature, and depth (CTD) sensor (*29*) continuously measures water levels in the western part of Dickson Fjord (Figs. 1C and 5B), its telemetered sampling interval of 15 min strongly aliases the short-period tsunamis and the ~90-s-period seiche (Fig. 4D). In addition, because the primary purpose of the CTD sensor located in the inner fjord was to detect calving events from the nearby Hisinger Glacier, our tsunami simulation hindcasts a much weaker seiche signal here, compared with the signal in the central segment of the fjord at the landslide (Fig. 5B and movie S2). Thus, the seiche signal recorded by this CTD sensor would have fallen to pre-event noise levels after only ~5 hours (Fig. 4D). Therefore, it is the distinctive combination of the tsunami simulation and seismic observations that corroborate the slowly decaying free seiche mechanism.

Although a previous study has reported earthquake tsunami–induced seiches persisting for several days in an island archipelago in the open ocean (*51*), the distinctively longer-duration and more slowly decaying VLP seismic signals documented in this study are likely related to the combination of a huge tsunami caused by a large fjord-transverse landslide and a highly confined water body in Dickson Fjord, with parallel shorelines. This effect is seen in the tsunami simulation, in which most seiche energy remains confined to the central segment of the fjord, with little leakage in- and out-fjord (Fig. 5B and movie S2). The sharp bend in the inner fjord seems to prevent propagation of the resonant wave components to the outer fjord system. This barrier effect is supported by the two independent tsunami modeling approaches (supplementary text S6). By contrast, the considerably more open fjord basins of Taan Fjord in Alaska and Karrat Fjord in West Greenland, with fjord-oblique slide directions, will have generated only weaker, shorter-duration seiches, as recorded in the corresponding near-field (<30-km) seismic observations (*28*, *52*).

Landslide tsunami–induced seiches must also have caused the five other, smaller VLP events. Two of these events were in winter, albeit with a slightly lower Q (table S1). Previous studies show that seiches can still occur in ice-covered water (*53*). During winter, the sea ice in the fjord is not completely fused to the coast, with a zone of tidal-induced fractures along the shore that can accommodate changing sea level with little energy dissipation (*54*).

The small deviation between the dominant frequency of the VLP (10.88 mHz) and simulated seiche (11.45 mHz) likely arises from uncertainties in the near-shoreline, shallow water bathymetry data (10% bathymetry difference based on analytical solutions) (*42*). This effect is shown by our tsunami simulation results using a coarser bathymetry dataset with 125-m spacing (*55*), which produced a larger, more discrepant dominant frequency of 12.45 mHz. Remaining minor differences between the decay rates of the observed VLP and synthetic waveforms could be attributed to unmodeled dissipation effects such as larger, high-amplitude waves breaking for the first cycles of the seiche (Figs. 4E and 5C)—which are not well-modeled with our hydrostatic numerical simulation (*56*) nonlinear frictional bottom stress (*51*, *57*, *58*)—and nonlinear water-seismic coupling and transmission along the walls of the fjord. Lastly, we propose that an observed tidal modulation of the VLP signal (fig. S14) occurs because a wider channel during higher tides outstrips the weaker channel-deepening effect, as per analytic solutions (*42*), thus reducing the fjord's eigenfrequency and associated VLP frequency. However, uncertain bathymetry close to the shoreline at shallow depths again prevents a detailed reconstruction of this effect from our numerical model.

In this study, we have focused on the monochromatic, dominant frequencies in the observed VLP seismic signal and the tsunami simulation. However, away from these dominant frequencies, these signals contain a set of weaker, yet discernible spectral peaks (Fig. 5, D and E), some of which are predicted overtones, whereas others are more enigmatic. For example, we identified a 90°-rotated radiation pattern in the first harmonic overtone compared with the fundamental. These weaker signals and their radiation patterns can be explored in more detail to further characterize this rare, unprecedented seiche event and to better understand how it transmits seismic energy into the solid Earth.

Conclusions and implications

Our study underscores intricate interconnections within the Earth system, specifically between the cryosphere, hydrosphere, and lithosphere. Our combined analyses, involving multiscale imagery, field data, tsunami simulations, and remote seismological data, demonstrate a complex, cascading chain of events in East Greenland. This sequence was originally preconditioned by climate change–induced glacial thinning, culminating, on 16 September 2023, in a large rockslide, which entered the fjord to generate a 200-m-high tsunami. The tsunami evolved into an initially 7-m-high, ~90-s-period freely oscillating seiche that decayed slowly owing to the confined nature of the fjord and could be detected seismically for 9 days. The large tsunamigenic rock-ice avalanche is an extraordinary event itself, the first ever recorded in East Greenland. Yet the 10.88-mHz monochromatic seismic signal highlighted an even more globally distinctive and puzzling phenomenon. We conclude that a tsunami stabilizing into a seiche is the mechanism driving this seismic signal. This conclusion comes from four key results: (i) the

near-identical frequencies (10.88 mHz versus 11.45 mHz) of the VLP signal and simulated seiche resulting from fjord geometry; (ii) a fjord-transverse oscillating single-force source that fits the VLP signal's radiation pattern and its absolute amplitude using a force value theoretically expected for the oscillating water body; (iii) the similar slow decay (Q ~10^3) of the simulated seiche and observed VLP signal; and (iv) the observed tidal modulation of the VLP seismic signal.

Even though seiches, in the presence of a persistent driving force [e.g., strong wind or storm events (*57*)], have previously been shown to be long-duration transient events or even continuous (*59*), our finding provides the first evidence of fluid sloshing, at a relatively short period of 90 s (compared with seiches in open oceans), persisting for several days without requiring an external driver. In particular, we have shown how seiches in narrow, deep, parallel-sided fjords can generate distinctive long-period, ultralong-duration seismic signals, which we would not have discovered without the combination of open data from global, high-quality, very-broadband seismic networks (*44*, *45*). Seismic detection and accurate localization of these events heavily depend on signal amplitude, period, and station noise levels.

The Dickson Fjord event also highlights the need for networks of high–sampling rate sea-level gauge sensors to be installed in confined basins across a wide range of geographic settings to directly record such events in the near field and in real-time (*60*). Specifically, such high-rate geophysical and hydrographic data from inside Dickson Fjord would be useful to record any further landslides and tsunamis with higher fidelity, to understand the spectral richness of the seismic signals and to detect any background resonances of the fjord. Our seiche simulations rely on high-resolution bathymetry models, thus presenting a global challenge for accurate tsunami modeling because such data are often missing in remote areas. As our study demonstrates, multidisciplinary collaboration is beneficial to unravel these cascading events and their unusual signals, and to map, rapidly assess, and mitigate associated destructive landslide-tsunamis.

REFERENCES AND NOTES

1. S. L. Gariano, F. Guzzetti, *Earth Sci. Rev.* **162**, 227–252 (2016).
2. S. T. McColl, *Geomorphology* **153–154**, 1–16 (2012).
3. C. K. Ballantyne, P. Wilson, D. Gheorghiu, À. Rodés, *Earth Surf. Process. Landf.* **39**, 900–913 (2014).
4. A. I. Patton, S. L. Rathburn, D. M. Capps, *Geomorphology* **340**, 116–128 (2019).
5. P. Saemundsson, C. Morino, S. J. Conway, in *Treatise on Geomorphology*, J. F. Shroder, Ed. (Academic Press, ed. 2, 2022), pp. 350–370.
6. C. B. Harbitz *et al*., *Coast. Eng.* **88**, 101–122 (2014).
7. F. Løvholt, G. Pedersen, C. B. Harbitz, S. Glimsdal, J. Kim, *Philos. Trans. A Math. Phys. Eng. Sci.* **373**, 20140376 (2015).
8. V. Heller, G. Ruffini, *Earth Sci. Rev.* **242**, 104459 (2023).
9. P. Poulain *et al*., *Geophys. J. Int.* **233**, 796–825 (2023).
10. B. Higman *et al*., *Sci. Rep.* **8**, 12993 (2018).
11. G. Lollino, A. Manconi, J. Locat, Y. Huang, M. Canals Artigas, Eds., *Engineering Geology for Society and Territory – Volume 4: Marine and Coastal Processes* (Springer International, 2014).
12. H. M. Fritz, F. Mohammed, J. Yoo, in *Tsunami Science Four Years after the 2004 Indian Ocean Tsunami: Part II: Observation and Data Analysis*, P. R. Cummins, K. Satake, L. S. L. Kong, Eds. (Birkhäuser, Basel, 2009), *Pageoph Topical Volumes*, pp. 153–175.
13. M. Geertsema *et al*., *Geophys. Res. Lett.* **49**, e2021GL096716 (2022).
14. T. Dahl-Jensen *et al*., *Nat. Hazards* **31**, 277–287 (2004).
15. K. Svennevig *et al*., *Sci. Total Environ.* **859**, 160110 (2023).
16. K. Svennevig *et al*., *Landslides* **19**, 2549–2567 (2022).
17. K. Svennevig *et al*., *Earth Surf. Dyn.* **8**, 1021–1038 (2020).
18. P. Favreau, A. Mangeney, A. Lucas, G. Crosta, F. Bouchut, *Geophys. Res. Lett.* **37**, L15305 (2010).
19. G. Ekström, C. P. Stark, *Science* **339**, 1416–1419 (2013).
20. C. Hibert, G. Ekström, C. P. Stark, *J. Geophys. Res. Earth Surf.* **122**, 1201–1215 (2017).
21. W. Chao *et al*., *Seismol. Res. Lett.* **89**, 1335–1344 (2018).
22. M. La Rocca *et al*., *Bull. Seismol. Soc. Am.* **94**, 1850–1867 (2004).
23. E. A. Kulikov, A. B. Rabinovich, R. E. Thomson, B. D. Bornhold, *J. Geophys. Res.* **101** (C3), 6609–6615 (1996).
24. J. M. Amundson *et al*., *Ann. Glaciol.* **53**, 79–84 (2012).
25. A. B. Rabinovich, in *Handbook of Coastal and Ocean Engineering*, Y. C. Kim, Ed. (World Scientific, 2009), pp. 193–236.
26. D. E. McNamara, A. T. Ringler, C. R. Hutt, L. S. Gee, *J. Geophys. Res.* **116** (B4), B04312 (2011).
27. L. Gualtieri, G. Ekström, *Geophys. J. Int.* **213**, 1912–1923 (2018).
28. A. Paris *et al*., *Pure Appl. Geophys.* **176**, 3035–3057 (2019).
29. Materials and methods are available as supplementary materials.
30. R. Delannay, A. Valance, A. Mangeney, O. Roche, P. Richard, *J. Phys. D Appl. Phys.* **50**, 053001 (2017).
31. A. Mangeney, *Nat. Geosci.* **4**, 77–78 (2011).
32. A. Dufresne *et al*., *Landslides* **16**, 2301–2319 (2019).
33. L. Moretti *et al*., *Geophys. J. Int.* **221**, 1341–1348 (2020).
34. C. Hibert, G. Ekström, C. P. Stark, *Geophys. Res. Lett.* **41**, 4535–4541 (2014).
35. L. Moretti *et al*., *J. Geophys. Res. Solid Earth* **120**, 2579–2599 (2015).
36. M. I. Arran *et al*., *J. Geophys. Res. Earth Surf.* **126**, e2021JF006172 (2021).
37. L. Moretti *et al*., *Geophys. Res. Lett.* **39**, L16402 (2012).
38. W. Boone, L. Ponsoni, G. Johnen, S. Rysgaard, "New technologies and insights from a real-time monitoring system of sea ice and oceanographic conditions in Northeast Greenland," EGU General Assembly 2023, Vienna, Austria, 24 to 28 April, Abstract EGU23-14430 (2023); https://doi.org/10.5194/egusphere-egu23-14430.
39. J. Macías, C. Escalante, M. J. Castro, *Nat. Hazards Earth Syst. Sci.* **21**, 775–789 (2021).
40. G. Davies, F. Romano, S. Lorito, *Front. Earth Sci. (Lausanne)* **8**, 598235 (2020).
41. D. Giles, E. Kashdan, D. M. Salmanidou, S. Guillas, F. Dias, *Comput. Fluids* **209**, 104649 (2020).
42. H. Q. Rif'atin, I. Magdalena, *J. Phys. Conf. Ser.* **1245**, 012061 (2019).
43. G. Pedersen, F. Løvholt, Documentation of a global Boussinesq solver, Preprint Series in Applied Mathematics 1, Dept. of Mathematics, University of Oslo, Norway (2008); https://www.ngi.no/globalassets/dokumenter/prosjekter/icg/globous-model-01-08.pdf.
44. A. T. Ringler *et al*., *Rev. Geophys.* **60**, e2021RG000749 (2022).
45. N. Leroy *et al*., *Seismol. Res. Lett.* **95**, 1495–1517 (2023).
46. B. P. Lipovsky, E. M. Dunham, *J. Geophys. Res. Solid Earth* **120**, 1080–1107 (2015).
47. S. Cesca *et al*., *Nat. Geosci.* **13**, 87–93 (2020).
48. H. Kanamori, J. Mori, *Geophys. Res. Lett.* **19**, 721–724 (1992).
49. R. Widmer, W. Zürn, *Geophys. Res. Lett.* **19**, 765–768 (1992).
50. A. M. Dziewonski, D. L. Anderson, *Phys. Earth Planet. Inter.* **25**, 297–356 (1981).
51. S. Allgeyer, H. Hébert, R. Madariaga, *Geophys. J. Int.* **193**, 1447–1459 (2013).
52. L. Gualtieri, G. Ekström, *Geophys. J. Int.* **213**, 1912–1923 (2018).
53. A. Farhadzadeh, *Ocean Eng.* **135**, 117–136 (2017).
54. L. Padman, M. R. Siegfried, H. A. Fricker, *Rev. Geophys.* **56**, 142–184 (2018).
55. P. Weatherall *et al*., *Earth Space Sci.* **2**, 331–345 (2015).
56. P. Poulain *et al*., *C. R. Geosci.* **354**, 361–390 (2022).
57. M. Bajo, I. Međugorac, G. Umgiesser, M. Orlić, *Q. J. R. Meteorol. Soc.* **145**, 2070–2084 (2019).
58. M. Okihiro, R. T. Guza, *J. Waterw. Port Coast. Ocean Eng.* **122**, 232–238 (1996).
59. J. Park, J. MacMahan, W. V. Sweet, K. Kotun, *Ocean Sci.* **12**, 355–368 (2016).
60. M. Heidarzadeh, A. Muhari, A. B. Wijanarto, *Pure Appl. Geophys.* **176**, 25–43 (2019).
61. S. Schippkus *et al*., ROBelgium/VLPGreenland: Accepted version, Zenodo (2024); https://doi.org/10.5281/zenodo.13221192.
62. W. Boone, S. Rysgaard, E. R. Frandsen, R. Develter, Flanders Marine Institute (VLIZ), Belgium, University Of Aarhus (AU), Denmark, Greenland Integrated Observatory - CTD & Atmospheric Station Dickson Fjord - 2023, Marine Data Archive (2023); https://doi.org/10.14284/637.

ACKNOWLEDGMENTS

We thank three anonymous reviewers and L. Toney for their time taken to provide excellent and constructive comments on the first version of the manuscript. We also thank B. Shiro and J. Carter for spending substantial time to improve the presentation of the manuscript. The Joint Arctic Command, the Sirius Dog Sled Patrol of the Kingdom of Denmark, and Northeast-Greenland Company Nanok are thanked for their cooperation and for making photos from after the event available to us. All initial and advanced scientific discussions were held virtually through the MatterMost platform. We are grateful to AskTom SCS for hosting this service. We are also grateful to W. Zürn for many fruitful and inspiring face-to-face discussions. We thank The Danish Agency for Data Supply and Infrastructure (SDFI) for providing GNET GNSS data. Any use of trade, firm, or product names is for descriptive purposes only and does not imply endorsement by the US Government. **Funding:** This research was supported by the Danish Energy Agency / DANCEA (Danish Cooperation for Environment in the Arctic) (K.S.); DT-GEO (A.M.) DN EnvSeis (A.M., E.S., and S.W.); Agence Nationale de la Recherche - ANR-20-CE01-0006 (C.H. and J.M.); PROMICE (N.J.K.); Agence Nationale de la Recherche - ANR-10-LABX-0023 (A.L.); Agence Nationale de la Recherche - ANR-18-IDEX-0001 (A.L.); the German Federal Ministry of Education and Research (BMBF) (S.S.); the Danish Ministry of Higher Education and Science - 5229-00005b (S.R.); the Aage V. Jensens Foundation - 30122021 (S.R., J.K., A.K.D., and E.R.); Horizon Europe - 101058129 (S.J.G., S.G., F.L., and A.M.); an IRD New Researcher grant (K.L.C.); the BELSPO Brain Project - B2/191/P1/GEOCAMB (R.D.); the Royal Society - URF\R1\180377 (P.K.); F.R.S.- FNRS through the MIS CalderaSounds funding - Fondation Wiener Anspach (C.C.); H2020 European Research Council - 802777-MONIFAULTS (P.P.); H2020 European Research Council (E.S.); MCIN/AEI/10.13039/501100011033/European Union NextGenerationEU/PRTR/ grant PDC2022-133663-C21 (M.C.); MCIN/AEI/10.13039/501100011033/ERDF "A way of making Europe" grant PID2022-137637NB-C21 (M.C.); the Doctoral School STEP'UP+ Agence Innovation Défense (N.D.P.D.); the Belspo BRAIN project - B2/191/P1/GEOCAMB (R.D.); NextGenerationEU - PID2022-137637NB-C22 (E.F.); H2020 European Research Council - 101001601 (A.M.G.F.); H2020 European Research Council - 852992 (A.-A.G.); Horizon Europe - 101093038, 101058129, 101058518 (A.-A.G.); National Science Foundation - EAR-2121568, EAR-2225286, OAC-2139536, OAC-2311208 (A.-A.G.); NASA - 80NSSC20K0495 (A.-A.G.); NOVO Nordisk foundation grant no. NNF23OC00807040 (S.A.K.); New Zealand MBIE via the Strategic Science Investment Fund Hazards and Risk Management program (O.D.L.); and the European Space Agency (J.M.). **Author contributions:** Conceptualization: K.S., S.P.H., T.L., F.L., and P.B. Data Curation: K.S., S.P.H., R.W.-S., N.J.K., A.L., R.E.A., S.S., S.R., W.B., P.H.V., B.L., E.C., T.D-J., R.D., L.G.E., M.K., J.K., S.A.K., and T.B.L. Formal Analysis: K.S., S.P.H., T.F., T.L., R.W.-S., A.M., C.H., N.J.K., A.L., C.S., R.E.A., S.S., S.R., W.B., S.G., F.L., A.M., A.L., T.T., P.K., C.E., W.D.H., D.G.C., C.C., E.S., P.H.V., F.C., T.D-J., N.D.P.D., A.D., L.G.E., M.H., M.K., S.A.K., A.K.D., T.B.L., J.-P.M., L.R., E.R.-C., S.W., and B.W. Funding Acquisition: S.R. and W.B. Investigation: K.S., S.P.H., T.F., T.L., R.W., A.M., C.H., N.J.K., A.L., C.S., R.E.A., A.M.,

S.S., S.R., W.B., S.J.G., K.L.C., S.G., F.L., K.V.N., J.D.A., A.M., A.L., T.T., M.S., P.K., C.E., A.C., W.D.H., D.G.C., C.C., E.L., E.S., P.H.V., T.D.-J., N.D.P.D., A.D., L.G.E., G.F., M.H., M.K., J.K., S.A.K., A.K.D., O.D.L., T.B.L., B.L., I.M., J.-P.M., L.R., E.R.-C., S.W., B.W., M.M., and K.V. Methodology: K.S., S.P.H., T.F., T.L., R.W.-S., A.M., C.H., C.S., R.E.A., S.S., S.J.G., F.L., A.M., and P.B. Projection Administration: K.S., S.P.H., T.L., and K.V.N. Resources: T.L., A.L., A.D., J.-P.M., and B.W. Software: K.S., S.P.H., T.F., T.L., R.W., A.M., A.L., C.S., R.E.A., A.M., S.S., S.J.G., F.L., A.M., E.S., M.J.C.-D., D.D., and E.D.F.-N. Supervision: K.S., S.P.H., and T.L. Validation: K.S., S.P.H., T.F., T.L., R.W., A.M., C.H., A.L., R.E.A., S.S., W.B., S.J.G., F.L., A.M., E.L., and E.R.-C. Visualization: K.S., S.P.H., T.F., T.L., R.W., A.M., C.H., N.J.K., A.L., C.S., R.E.A., A.M., S.S., S.R., W.B., S.J.G., K.L.C., S.G., F.L., J.D.A., A.M., A.D., L.G.E., S.A.K., L.R., and E.R.-C. Writing (original draft): K.S., S.P.H., T.F., T.L., R.W., A.M., C.H., R.E.A, A.M., S.S., S.R., W.B., S.J.G., S.G., F.L., L.G.E., A.K.D., and E.R.-C. Writing (review and editing): K.S., S.P.H., T.F., T.L., R.W., A.M., C.H., N.J.K., A.L., C.S., R.E.A., A.M., S.S., S.R., W.B., S.J.G., K.L.C., S.G., F.L., K.V.N., J.D.A., A.M., A.L., T.T., M.S., R.D., P.K., A.C., W.D.H., D.G.C., P.P., E.L., E.S., P.H.V., B.L., F.C., R.D., L.G.E., A.M.G.F., G.F., A.-A.G., A.L.K., J.K., A.K.D., O.D.L., B.L., I.M., L.R., E.R.-C., and S.W. **Competing interests:** The authors declare that they have no competing interests. **Data and materials availability:** We provide a publicly available Zenodo repository (*61*) that comprises materials, data, and code to allow the main findings and figures of this paper to be reproduced. Data from the Dickson Fjord sea-level gauge/CTD and meteorological station are also publicly available (*62*). All other seismic and remote sensing data come from publicly available repositories (see materials and methods) for each FDSN network code and corresponding citation). The Global Seismographic Network (GSN) is a cooperative scientific facility operated jointly by the NSF and the United States Geological Survey (USGS). The NSF component is part of the NSF SAGE Facility, operated by EarthScope Consortium under Cooperative Agreement EAR-1724509.

SUPPLEMENTARY MATERIALS

Submitted 9 January 2024; resubmitted 19 June 2024
Accepted 6 August 2024
10.1126/science.adm9247